Materials for life sciences

Nanocomposites based on hydroxyapatite/lithium oxide and graphene oxide nanosheets for medical applications

M. Afifi[1,2], Mehrez E. El-Naggar[3,*] , Shabbir Muhammad[4,5], Noweir Ahmad Alghamdi[6], S. Wageh[7,8], Salem R. Salem[9], Dalal Alhashmialameer[10], and Manal Abou Taleb[11,12]

[1] Ultrasonic Laboratory, National Institute of Standards, Giza, Egypt

[2] Faculty of Nanotechnology for Postgraduate Studies, Cairo University, El-Sheikh Zayed, Giza 12588, Egypt

[3] Institute of Textile Research and Technology, National Research Centre, El behouth Street, Dokki 12622, Giza, Egypt

[4] Research Center for Advanced Materials Science (RCAMS), King Khalid University, P.O. Box 9004, Abha 61413, Saudi Arabia

[5] Department of Chemistry, College of Science, King Khalid University, P.O. Box 9004, Abha 61413, Saudi Arabia

[6] Department of Physics, Faculty of Science, Albaha University, Alaqiq 65779, Saudi Arabia

[7] Department of Physics, Faculty of Science, King Abdulaziz University, Jeddah 21589, Saudi Arabia

[8] Physics and Engineering Mathematics Department, Faculty of Electronic Engineering, Menoufia University, Menouf 32952, Egypt

[9] Department of Biochemistry and Clinical Biochemistry, Military Medical Academy, Cairo, Egypt

[10] Department of Chemistry, College of Science, Taif University, Taif 21944, Saudi Arabia

[11] Department of Chemistry, College of Science and Humanities, Prince Sattam Bin Abdulaziz University, Al-kharj, Al-Kharj 11942, Saudi Arabia

[12] Department of Polymer Chemistry, National Center for Radiation Research and Technology (NCRRT), Egyptian Atomic Energy Authority, P.O. Box 7551, Nasr City, Cairo 11762, Egypt

ABSTRACT

Metal-based bioceramics are developed to imitate the natural bones to be used as bone substitutes. Different nanocomposites are synthesized using hydroxyapatite (HAP), Li_2O and GO to fabricate HAP, Li_2O, HAP/Li_2O, HAP/GO and HAP/Li_2O/GO. XRD shows the change in crystal structure upon adding the three nanocomposites to each other. Besides, FTIR and XPS explain the functional groups of the compositions and analyze their surface composition. The TEM explains the morphological changes for particles dimensions of HAP/Li_2O/GO showing a length of 20 nm for HAP and a size of 6 nm for Li_2O sphere. In addition, SEM graphs explained the enhancement of HAP/Li_2O/GO porosity showing a particle size of 0.3–0.4 μm and length of 0.8 μm. Further,

Handling Editor: Annela M. Seddon.

Address correspondence to E-mail: mehrez_chem@yahoo.com

roughness parameters are improved upon adding HAP and Li_2O to GO, showing a roughness average value of 57.80 nm. Moreover, the cell viability of HAP/Li_2O/GO is examined and shows a maximum value of $97.4 \pm 1.2\%$. In addition, the antibacterial activity exhibited by HAP/Li_2O/GO against (*Escherichia coli* = *E. coli*) and (*Staphylococcus aureus* = *S. aureus*) showed an inhibition zone of 13.4 ± 1.2 mm 12.3 ± 1.3 mm. Adding HAP presents an improvement in surface roughness as well as cell viability and antibacterial activity. Besides, the microhardness has been improved from 2.6 ± 0.1 GPa to 3.1 ± 0.2 for pure HAP and HAP/Li_2O/GO, respectively. Therefore, combining HAP, GO and Li_2O results in a nanocomposite of enhanced biocompatibility and can be suggested for bone biomedical applications.

Introduction

Major bone injuries lead to disabilities and affect the quality of life [1]. Tissue engineering has been used widely in to develop new biomaterials that can act as implant materials to accelerate the bone repairing process [2, 3]. Modulating biomaterial's grain size, surface roughness and porosity surprisingly enhances their bioactivity and biocompatibility [4]. Bioscaffolds containing metal ions are one of the promising biomaterials for bone replacement applications [5, 6]. Bone is a combination of organic materials mainly collagen fibers and inorganic materials such as hydroxyapatite [7–9].

Hydroxyapatite (HAP) is a bioceramic material that imitates native bone apatite [10–12]. It was studied in bone defects as an implant material due to its osteoconductive and biocompatible ability [13–15]. Regardless of HAP advantages, it cannot be used as a single biomaterial for high load-bearing applications due to its poor mechanical strength [8, 16, 17]. Nie et al. studied the effects of graphene oxide (GO) concentrations into HAP [18]. Their study illustrated that the composition showed better mechanical parameters and enhanced proliferation. Moreover, Nosrati et al. studied HAP/GO [19–21]. Further, Nunez et al. explained the role of GO in improving HAP biocompatibility and bioactivity [22]. The biomedical applications of HAP are not only for bone engineering but also used in wound healing applications. Yu et al. HAP in a composite of alginate hydrogel and simvastatin for wound healing applications. It was found that wound closure is higher with using the composite by around 20% than using normal saline [23].

Graphene oxide (GO) is a single layer of sp^2 carbon bonding to each other forming a honeycomb shape [24]. GO possesses numerous surface oxygen-containing, functional groups, these groups improve its bonding to the biomolecules [25]. Further, GO exhibits corrosion stability properties [26]. Rajesh et al. explained the improvement in biocompatibility and osteoinductivity of HAP upon adding GO [27]. Moreover, Shin et al. illustrated the improvement in the osteogenesis process after adding GO to HAP [28]. In addition, Shuai et al. revealed the enhancement of HAP porous structure after adding GO [29]. They explained that this improvement in porosity played a crucial role in passing nutrients and inducing cell attachment and proliferation.

On the other hand, lithium (Li) has been examined for various applications [30]. It was proved that lithium-containing biomaterials possessed the better osteoconductive ability, besides had a role in the bone formation process [31]. Moreover, Li could be considered as a trace element that can promote the proliferation of stem cells and osteogenic differentiation [32, 33].

It could be reported that Wang et al. showed an improvement in HAP properties upon substitution with lithium ions [34]. They illustrated that Li substitution improved HAP osteoconductivity and enhanced its strength. Furthermore, Popescu et al. examined the substitution of HAP with Li ions [35]. They explained that Li substituted HAP showed better biocompatibility and promoted cell adhesion and proliferation. Furthermore, Keikhosravani et al. tested the antibacterial of HAP modified with different contributions of Li ions (0.0, 0.5, 1.0, 2.0, 4.0) wt%. They found that the behavior of against E. coli was more than S. aureus [36]. However, the highest

contribution of Li ions does not exceed 4.0 wt% to avoid the formation of secondary phases. Therefore, manipulating nanocomposites with high contributions of each component could be better to achieve high physicochemical behaviors of the resultant composite than the dopant ones. For instance, the development of the mechanical properties of HAP might occur with the addition of Li_2O, which also possesses a relatively low density than pure HAP. Thus, in the current study, Li_2O could be suggested to be used with much higher contributions reaching around 40–50 wt%. In addition, the gathering of these nanoparticles introduce a simple mechanism for each composition to overcome the other's drawbacks [37]. The GO can act as a reinforcement agent or as a matrix, while both HAP and Li_2O are the fillers that are embedded through the nanosheets of GO. This structural configuration might offer a manipulated composition with distinctive properties to be appropriate for medical usage. The insertion of Li_2O to investigate its biocompatibility with HAP and to increase the poor antibacterial activity of HAP. Abdel-Wahed et al. prepared glass based on Li_2O and recommended it to be used in biomaterial applications [38]. Furthermore, Aminitabar et al. synthesized a bioglass composite containing Li_2O. They investigated its biocompatibility in vitro toward osteoblast cells and the optical density value doubled in 3 days which indicates the high biocompatibility [39]. Moreover, GO is added to improve the properties of HAP and to bind the two phases of HAP and Li_2O on the surface of nanosheets of GO.

This work's purpose is to synthesize a triple nanocomposite containing HAP, Li_2O and GO to be utilized as bone implant material in bone defects. $HAP/Li_2O/GO$ is examined with various scans and analyses to show the surface alteration that occurred. Besides, it is assessed for its antibacterial activity and corrosion resistance.

Materials and methods

Precursors

$CaCl_2.2H_2O$, $(NH_4)_2HPO_4$, Li_2O, graphite, HCl and KMnO4 were purcahsed from LOBA, India.

Synthesis procedure

First, HAP synthesis was prepared as follow: two beakers to prepare 0.5 M of $CaCl_2.2H_2O$ and 0.3 M of $[(NH_4)_2HPO_4]$. Then, the (P) solution was added to (Ca) drop-wise. The pH reaction was maintained at 11 ± 0.1 by using diluted ammonia. Afterward, the (P) was added slowly to the (Ca) beaker. Then a magnetic stirrer was needed for 2 h to mix the solution. Then, the solutions were left for 24 h to age. The formed gel was filtered and washed. The filtered gel was dried.

Second, the synthesis of GO was carried out using a modified Hummers technique [40]. Add 5 g graphite to 120 mL of H_2SO_4 in a vessel and vigorously stirred for 30 min. Then, in the graphite jar, 12 g of $KMnO_4$ was added and stirred for another 2 h. Due to the potential for an increase in temperature, 300 mL of DIW was introduced at a rate of 10 mL/h throughout this reaction. After allowing the solution to cool, gently poured in 10 mL of H_2O_2 and aggressively stirred for 30 min. Using an ultrasonic probe, the mixture was disseminated numerous times using 500 mL of HCl (20 wt%) for 15 min.

Then, prepare the samples as (a) pure HAP, (b) pure Li_2O, (c) $HAP:Li_2O = 1:1$, (d) 1 g HAP/ 0.05 g GO and (e) 1 g $HAP/1$ g $Li_2O/0.1$ g GO.

The three components (HAP, Li_2O and GO) were mixed in ethanol surrounded by crushed ice (10 °C). It was noted that the chemical stability of Li_2O in ethanol is substantially greater than that of distilled water, and the low temperatures were set to minimize the excessive ethanol evaporation during the sonication process. Prepare five tubes, each with 50 mL of ethanol in them. After that, each nanocomposite was weighted and placed it in one of the five tubes. Then, for 15 min, each tube was placed in the probe sonicator to equally spread the solution. Following that, the powder samples in each tube were centrifuged for 10 min at 6000 r.p.m. Finally, the samples were dried at 50–60 °C for several hours. While the PVA solution was dumped to generate uniform muddy powder, the powder was squeezed into a desk shape in a coaxial stainless steel mold for such disks. Then, following compression, it was heat-treated at 350 °C to remove any particles. Figure 1 shows the acquired samples.

Figure 1 Photograph showing the shape of the obtained powder which are from the left: HAP, Li$_2$O, HAP/Li$_2$O, HAP/GO and HAP/Li$_2$O/GO.

Instrumental measurements

Pertpro, Cu k$_{\alpha 1}$ radiation (λ = 1.5404 Å) record the XRD. The preparation of the sample for the X-ray test is based on putting a fine powder of the sample through the X-ray holder, then closing the window to start scanning. The scanning was done at room temperature from 2theta = 10 $^\circ$ to 70 $^\circ$, with a step of 0.02° and a step size around 0.5 s. In addition, the Fourier transformer infrared (FTIR) spectrum was reported at the range of 4000–400 cm^{-1} via FTIR spectrometer (PerkinElmer 2000). The resolution was around 0.5 cm^{-1}. The test was done as

1- 2 g of each sample.
2- Each sample was added to KBr (20:1).
3- The sample is pressed using uni-axial pressure.
4- The test was done.

Moreover**,** PerkinElmer PHI 5600 is the XPS instrument. In addition, FESEM, model QUANTA-FEG250 (the Netherlands) was used to study the surface features. The high voltage was adjusted to around 10 kV. Furthermore, Gwyddion 2.4 software was used to process the SEM images. The resolution of the obtained SEM images is fixed at 900 × 1400 pixel, while the boundaries of the images were cut. Then, the processing of the image could produce both 3D images. The x and y axis in the 3D images are similar to their analog in SEM images, however, the roughness parameters were taken from the z-axis. In addition, these values were taken as relative values between the studies samples. The images were not calibrated and were used as they obtained from the software for relative comparison.

In vitro cell viability tests

The cell line that obtained from AmericanType Culture Collection (ATCC, Manassas, VA, USA) was used under culturing conditions in Dulbecco's modified Eagle's medium (DMEM, Gibco) to examine cell viability. Cells with a density of 5 × 10^3 (cells/cm^2) were cultured on the composites through 24-well plates, then they were incubated at 37 °C. After three days the MTT was added into and the cell viability was detected [40–42].

Antibacterial activity

The antimicrobial activity was done using the diffusion desk method against (*Escherichia coli* = *E. coli*) and, (*Staphylococcus aureus* = *S. aureus*). Concentrate the powdered samples to about 20 mg/mL. The samples were left with the two pathogens for 24 h; afterward, the inhibition zone was measured.

Corrosion study

The electrochemical performance of the nanocomposites was studied by measuring their degradation in SBF. This degradation investigation was carried out using the Open Circuit Potential (OCP). The samples were formed as cylindrical disks having a diameter of about 5 mm and a thickness of about 3 mm. The SBF solution was used to submerge and fix the other surface.

Results and discussion

Phase identification

Figure 2 shows the XRD patterns of different nanocomposites. The characteristic peaks of HAP that explain its hexagonal crystal structure appeared at $2\theta = 25.8°, 31°, 33°, 40°, 47°, 50°, 53°$ which are attributed to the planes (002), (211), (300), (310), (222), (213) and (004), respectively [43, 44]. The most significant peak of GO at $10°$ is low. This lowering explains the anchoring of Li_2O and HAP with GO sheets [45]. Further, lithium characteristic peaks appear at 32°, 35.5°, 36.13°, 51.48°, these sharp peaks indicate the high crystallinity of Li_2O [46]. The low peak intensity of the peak at $2\theta = 20°$ proves the presence of lithium phosphate which indicates the interaction between HAP and Li_2O [47]. The sharp signals that appeared in the XRD show the purity and crystallinity of the nanoparticles [48].

FTIR spectra

Figure 3 represents the FTIR of HAP, Li_2O, HAP/ Li_2O, HAP/GO and HAP/Li_2O/GO compositions. Table 1S reports the significant bands of the spectra. The main band of GO is around 3430 cm^{-1}, which is assigned to the vibration of O–H, while the band of 2940 cm^{-1} is attributed to the C-H bond in sp^3 hybridization. The band of 1620 cm^{-1} refers to the stretching mode of the carbon network (C=C) which belongs to sp^2 hybridization [49]. The lowest band at 503 cm^{-1} refers to asymmetric stretching vibration of Li–O [50]. Moreover, the characteristic bands of the HAP phosphate group appear at $550–605$ cm^{-1} ascribed for the asymmetric bending mode (ν_4), in addition to the asymmetric (ν_3) that appeared at $1020–1090$ cm^{-1} [51–53]. Moreover, the aromatic C=C vibration of GO appeared at 1634 cm^{-1} [54]. Besides, the peak at 1417 cm^{-1} is assigned for CO_3^{2-} group due to the interaction with ambient air [55]. Further, the O–H vibration was at $3457–3464$ cm^{-1} [56]. The carbonated HAP looks more biocompatible than the pure one [57]. Moreover, the hydroxyl ions prefer to bond with the cells, which can give more affinity to the implant material [58].
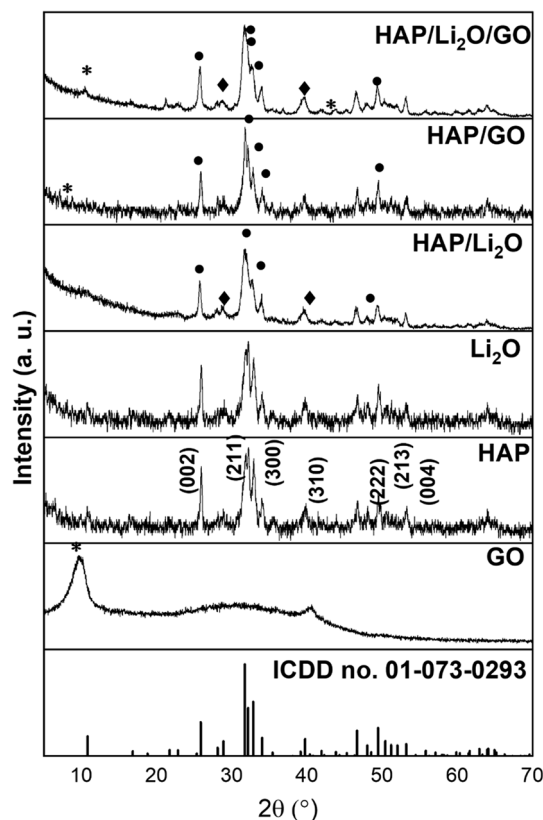
Figure 2 XRD pattern of different samples: HAP, Li_2O, HAP/ Li_2O, HAP/GO and HAP/Li_2O/GO; (•) HAP, (◆) Li_2O and (*) GO.

XPS spectra

The elemental of HAP/Li_2O/GO is explained in XPS spectra in Fig. 4, while Table 1 represents the different binding energies for the significant appeared bands. Figure 3a shows the survey scan of HAP/ Li_2O/GO that reveals the presence of Li, Ca, P, C and O. The presence of all these elements proves the uniform distribution and the presence of the compounds of Li_2O, HAP and HAP. Figure 3b represents the C 1 s scan, showing peaks at binding energy 284 eV, 285.5 eV and 290 eV that are assigned to C = C, C–O and HO-C = O [59, 60]. Moreover, the O 1 s scan is displayed in Fig. 3c in which the significant bands appeared at 531.5 eV that were assigned to C = O and O = C–OH, besides the peak at 532.3 eV that was attributed to C–OH and 533.1 eV that ascribed to P = O [61–64]. Furthermore, Fig. 3d shows the Ca 2p scan that demonstrates the significant two peaks of Ca 2p$_{3/2}$ and Ca 2p$_{1/2}$ at a binding energy of 348 eV and 351.6 eV [51, 65]. In addition, the P 2p scan shown in Fig. 3 e reveals the single

characteristic peak of P 2p$_{1/2}$ at 134 eV [51, 65]. Figure 3f demonstrates Li 1 s scan that shows Li significant peak at 57.4 eV [66]. These findings in addition to XRD and FTIR results confirm that there is no chemical interaction of GO nanosheets HAP and Li$_2$O.

Morphological features

TEM graphs are in Fig. 5a–e to further explain the morphological features. Figure 5a shows the typical HAP aggregated nanorods with a length of 20–100 nm. Further, Li$_2$O single spherical particle is shown in Fig. 4b with a diameter size of 100 nm. Figure 4c illustrates the reduction in HAP rods diameter to be 8–14 nm and length of 25–50 nm after addition Li$_2$O. Moreover, Li$_2$O particle size notably decreased to 14 nm. Adding GO to HAP shows a rod size of 4–11 nm that is anchored within GO nanosheets that are illustrated in Fig. 5d. The triple nanocomposite is explained in Fig. 5e showing the scattered HAP nanorods and Li$_2$O nanoparticles over GO nanosheets with a remarkable reduction in size and length of the nanoparticles to show 6 nm diameter and 20 nm length for HAP and 6 nm size of Li$_2$O sphere. TEM graphs together with XPS scan show the uniform and strong binding between HAP, Li$_2$O and GO sheets.

Materials in the nanoscale could be obtained via two main approaches: down–up and up–down. The up–down track is considered a physical technique when the large particles are crushed/dispersed to be smaller than their initial state. This could be done via a powerful ultrasonic probe, which was able not only to combine the ternary nanocomposites together in the nanoscale, but it was also able to reduce their size distribution. Furthermore, it is difficult to obtain

statistical data to be analyzed for the distribution of the particles from images, but it could be hypothesized that the ternary nanocomposites, their particle shape, size and topography, have been influenced significantly by the powerful probe sonicator [67, 68].

Figure 6a–d shows the SEM graphs of HAP, HAP/ Li$_2$O, HAP/GO and HAP/Li$_2$O/GO. Figure 6a illustrates the typically aggregated nanorods of HAP with a diameter size of 0.3–0.8 μm and a length of 1.1–4.6 μm. Further, HAP/Li$_2$O is shown in Fig. 6b, adding Li$_2$O to HAP shows a HAP clustering and distribution of Li$_2$O particles over HAP rods. HAP nanorods exhibit a reduction in diameter size of 0.1–0.5 μm and length of 0.8–4 μm. In addition to the fluffy spherical pattern of Li$_2$O that shows a grain size of 0.5–0.8 μm. Moreover, Fig. 6c presents HAP/ GO which represents the incorporation of HAP rods
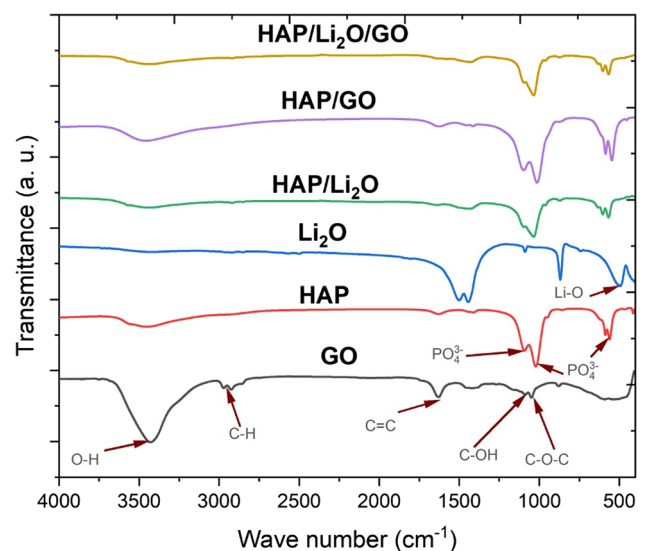
Figure 3 FTIR spectra for GO, HAP, Li$_2$O, HAP/Li$_2$O, HAP/GO and HAP/Li$_2$O/GO.

Table 1 XPS bands for HAP/Li$_2$O/GO samples

Bond	Binding energy (eV)	Atomic (%)	Assignment	Ref
P 2p	134	100	P 2p$_{1/2}$	[51, 65]
C 1 s	284	17.36	C = C	[59]
	285.5	56.79	C–O	[59]
	290	25.85	HO–C = O	[60]
Ca 2p	348	68.57	Ca 2p$_{3/2}$	[51, 65]
	351.6	31.43	Ca 2p$_{1/2}$	[51, 65]
O 1 s	531.5	44.41	C = O/O = C–OH	[64]
	532.3	28.77	C–OH	[64]
	533.1	26.81	P = O	[61–63]
Li 1 s	57.4	100	Li$_2$O	[66]
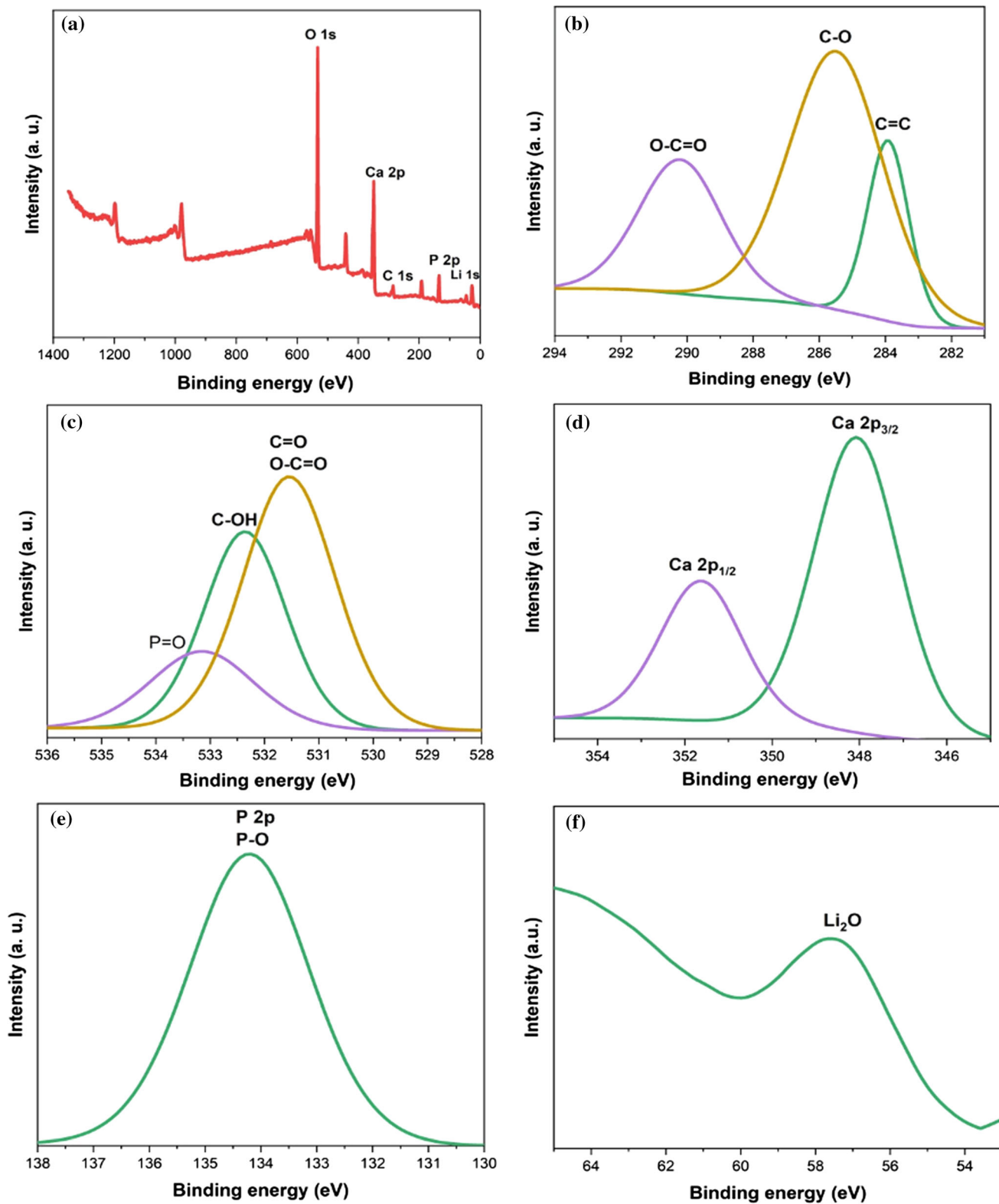
**Figure 4** XPS of HAP/Li$_2$O/GO: **a** survey scan, **b** C 1 s, **c** O 1 s, **d** Ca 2p, **e** P 2p, **f** Li 1 s.

within GO nanosheets with a size of 0.3–1.2 μm and a length of 1–3 μm. However, adding HAP and Li$_2$O to

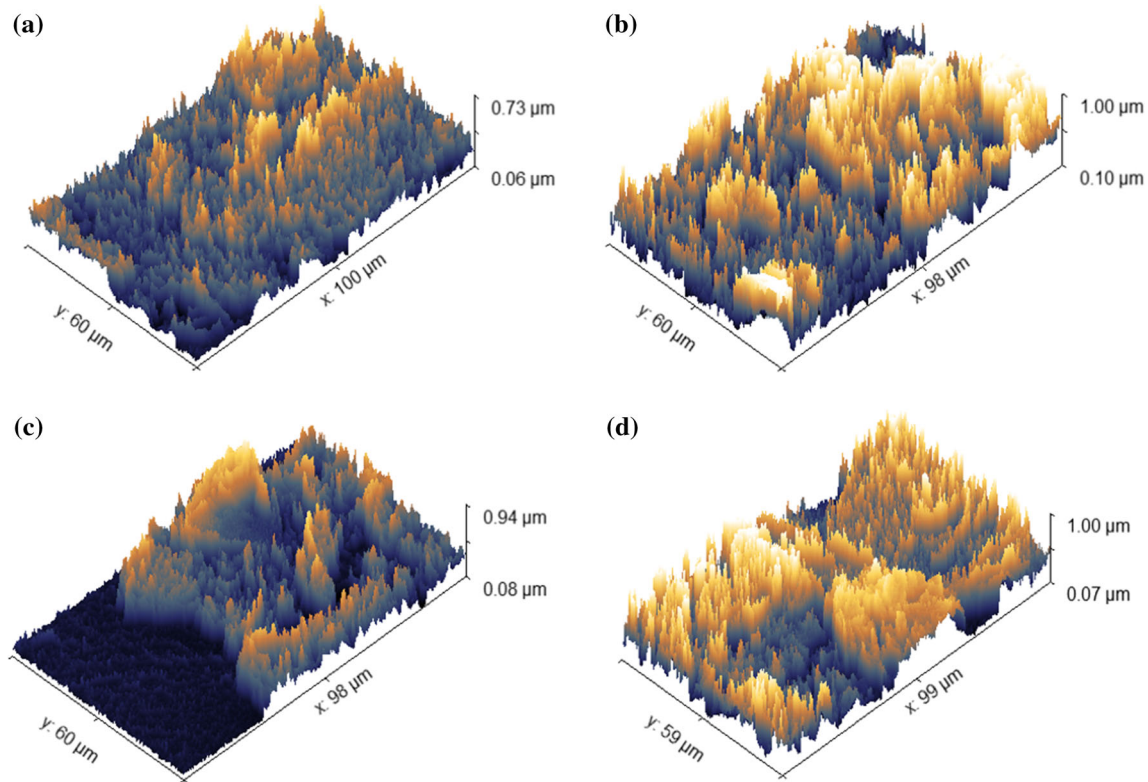GO sheets is explained in Fig. 6d which displays the uniform incorporation of all nanoparticles with each
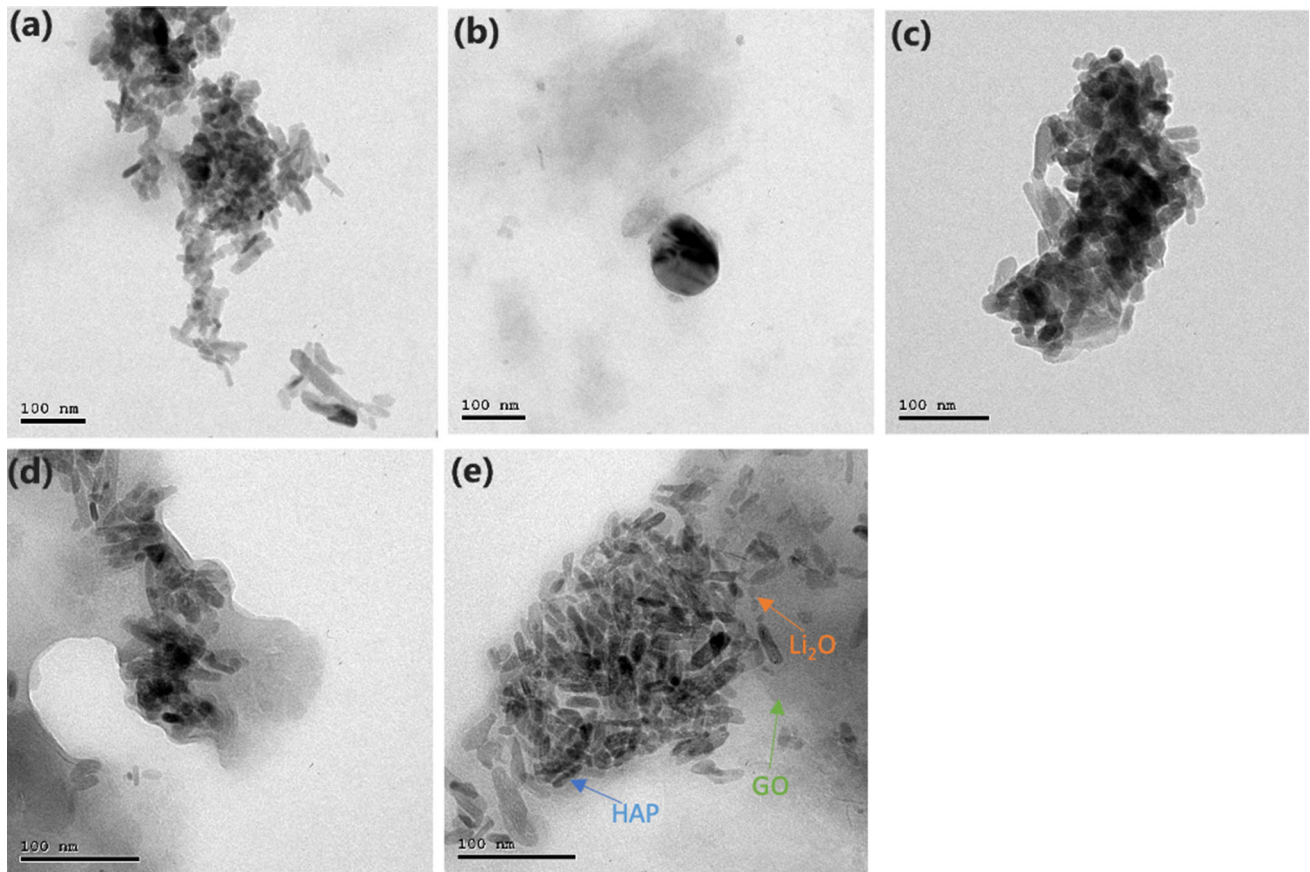
Figure 5 TEM of **a** HAP, **b** Li_2O, **c** HAP/Li_2O, **d** HAP/GO and **e** HAP/Li_2O/GO.

Figure 6 SEM micrographs of **a** HAP, **b** HAP/Li_2O, **c** HAP/GO and **d** HAP/Li_2O/GO.

(a)

(b)

(c)

(d)
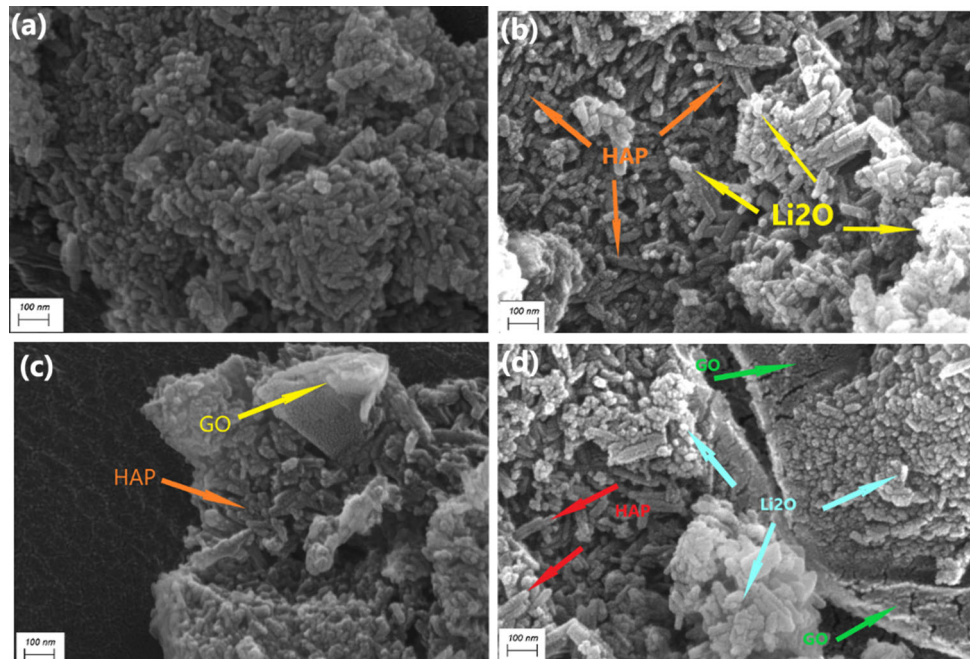
Figure 7 surface roughness of **a** HAP, **b** HAP/Li$_2$O, **c** HAP/GO and **d** HAP/Li$_2$O/GO.

**Table 2** Parameters of surface roughness for HAP, HAP/Li$_2$O, HAP/GO and HAP/Li$_2$O/GO

Compositions	Ra (nm)	Rq (nm)	Rt (nm)	Rv (nm)	Rp (nm)	Rtm (nm)
HAP	28.69	37.46	276.50	133.71	142.78	203.88
HAP/Li$_2$O	52.70	69.57	465.19	243.71	221.48	309.28
HAP/GO	29.86	42.37	320.43	161.35	159.07	214.71
HAP/Li$_2$O/GO	57.80	75.85	526.58	260.49	266.09	391.45

other. GO sheet appeared as a cracked surface evenly anchoring HAP and Li$_2$O particles showing an average diameter size of 0.3 μm and 0.4, respectively. Besides, HAP average rod length of 0.8 μm. This unique pattern of HAP/Li$_2$O/GO reveals a grain size reduction that results in a high surface area which enhances the porosity of the composition and consequently improves its biocompatibility.

It could be noticed that a large difference in particle size was obtained between SEM and TEM. The difference is assigned to the technique of sample preparation from both SEM and TEM. In other words, the preparation of samples for TEM imaging includes a powerful sonication of the powder through deionized water. Then, the copper grid is immersed for seconds to collect suspended particles to be investigated. On the other hand, the powder

sample is input into SEM for scanning without significant changes. Therefore, this scenario allows the particle to be agglomerated and combined in a low area [69, 70].

The modulation of surface roughness is explained in Fig. 7a–d, whereas Table 2 represents the modified roughness parameters. The roughness (Ra) varies from 28.69 nm to 52.7 nm and 29.86 nm for HAP, HAP/Li$_2$O and HAP/GO, respectively, reaching the maximum Ra value of 57.8 for HAP/Li$_2$O/GO. Further, the root mean square (Rq) changes from 37.46 nm for HAP to 69.57 nm and 42.37 nm for HAP/Li$_2$O and HAP/GO. Adding HAP and Li$_2$O to GO improves (Rq) value to be 75.85 nm. Moreover, the maximum height (Rt) increased from 465.19 nm and 320.43 nm for HAP/Li$_2$O and HAP/GO to the highest value of 526.58 nm for HAP/Li$_2$O/GO.
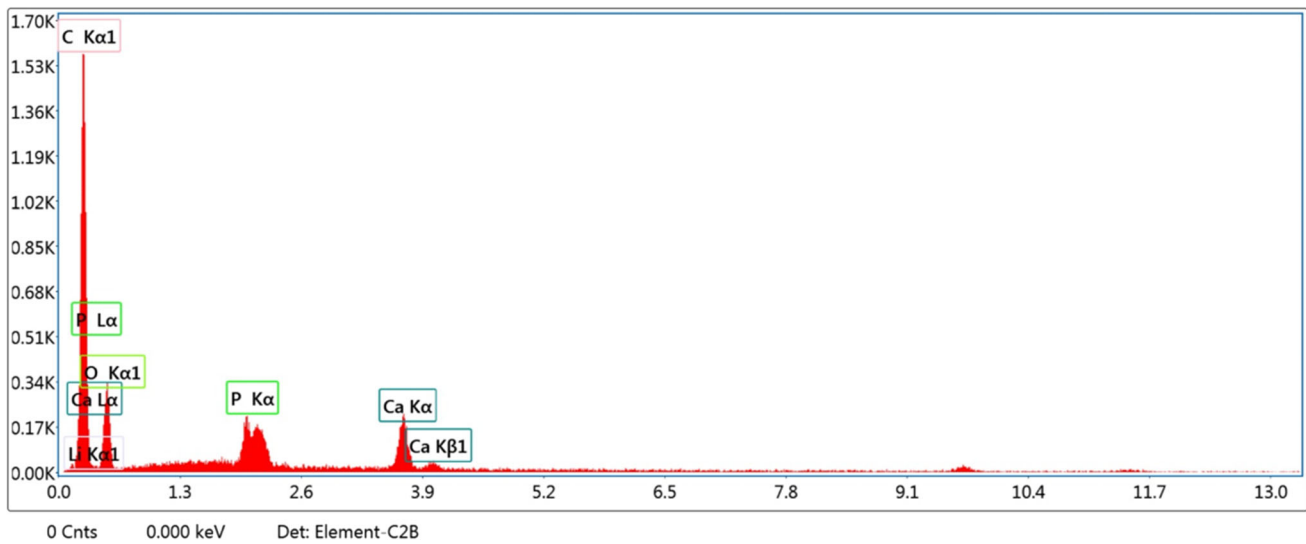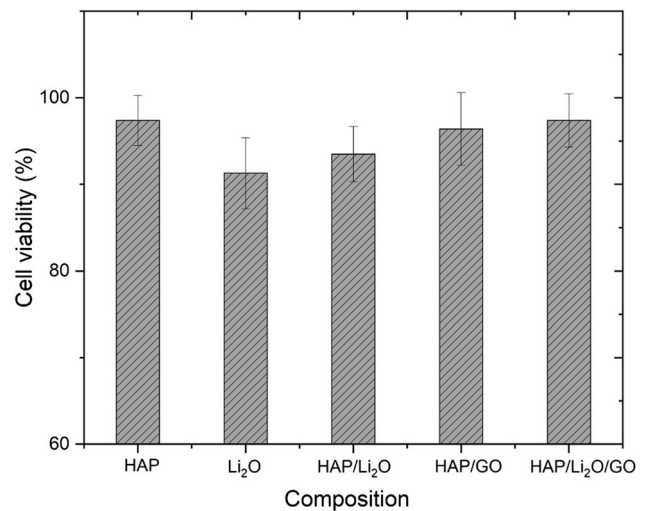
Figure 8 EDX spectrum of HAP/Li$_2$O/GO.

Table 3 Elemental composition values of HAP/Li$_2$O/GO nanocomposite

Element	Weight %	Atomic %
C K	61.46	70.54
O K	24.42	21.05
P K	4.52	2.01
CaK	7.71	2.65
LiK	1.89	3.75

Figure 9 Cell viability of human osteoblast cell line for HAP, Li$_2$O, HAP/Li$_2$O, HAP/GO and HAP/Li$_2$O/GO.

Furthermore, the highest value of maximum valley depth (Rv) is 260.49 nm which is obtained by HAP/Li$_2$O/GO. In addition to the improvement of maximum peak height (Rp) and an average maximum height (Rtm) values reach a maximum value of 266.09 nm and 391.45 nm for the triple nanocomposite. The alteration of surface topology and surface roughness proved with SEM micrographs indicates the enhancement of porous structure and biocompatibility of the ternary composition HAP/Li$_2$O/GO. Hence, HAP/Li$_2$O/GO nanocomposite is suggested as an implanted biomaterial. The roughness development refers to the increase of surface area. Therefore, the active sites of adhesion are increased [71–73]. According to the mechanical theory of adhesion, the shape of the surface, such as deep valleys and heights in the implant, can induce mechanical interlock [63, 74].

It was reported by Müller that biocompatibility could be tailored via surface topography. In other words, enlargement of morphological values induce roughness which promote the notches and heights [75]. These peaks can attract proteins for interaction and thus promoting biocompatibility. The presence of a high ratio of porosity might induce high surface defects [76, 77].
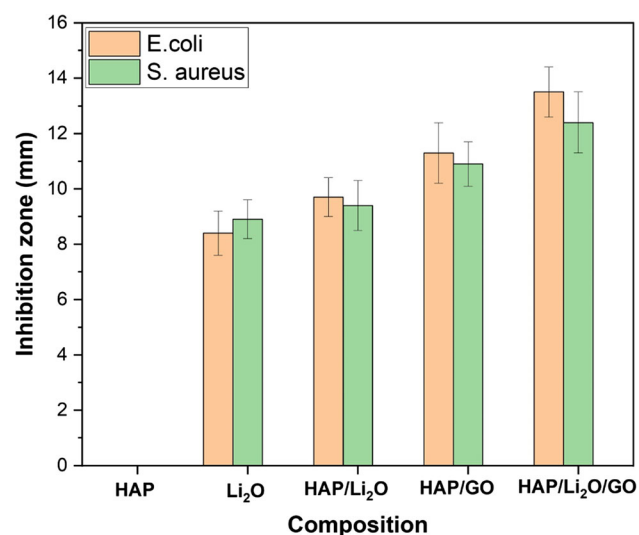
EDX analysis

Figure 8 illustrates the EDX spectra of HAP/Li$_2$O/GO that represent the surface elemental composition of the nanocomposite. While Table 3 reports the values of the elemental composition in the form of atomic and weight percentages. The spectrum

displays intense peaks assigned to the presence of Li, Ca, C, O, P elements. The appearance of all the elements indicates the even distribution of HAP and Li_2O within GO sheets. In addition, the Ca/P ratio is 1.7 and the C/O ratio is 0.3, these ratios prove the presence of HAP and GO, respectively [78, 79]. Further, the Ca/P ratio imitates the natural bone apatite ratio which suggests this nanocomposite to be utilized in bone repair applications [80].

Cell viability

The cell viability is evaluated using a human cell line. Figure 9 demonstrates the cell viability values of HAP, Li_2O, HAP/Li_2O, HAP/GO and HAP/Li_2O/ GO. It is noted that HAP shows a high viability value of $97.3 \pm 0.8\%$ and this is related to the high osteoconductive ability of HAP [13]. Further, Li_2O exhibits the lowest viability value in the evaluation of $91.3 \pm 0.9\%$. However, adding HAP to Li_2O shows a slight enhancement in viability value to be $93.5 \pm 1\%$. Moreover, adding HAP to GO reveals also a high viability value of $96.3 \pm 1.1\%$. Combining the nanoparticles of HAP/Li_2O/GO exhibits the highest ratio of living cells of $97.4 \pm 1.2\%$. It was found that the change of compositions causes a statistically measurable effect on the degree of cell viability ($p = 0.0502$).

In the ternary nanocomposite, the Li_2O is dispersed between the particles of HAP and the nanosheets of GO. This might shade the effects of Li_2O partially. In addition, the incorporation of Li_2O nanoparticles within the composite of HAP/GO might cause a crumbling of the particles, which enlarges the surface area and could enhance the cell viability. Furthermore, the osteoconductive ability of Li was proved by Masaki Arioka et al., so that Li has a role in bone mineralization and formation process [81]. Herein, HAP/Li_2O/GO nanocomposite can be suggested for bone replacement applications.

Antibacterial activity

The antibacterial of the samples is assessed against two bacteria: *E. coli* and *S. aureus*. Figure 10 illustrates the toxicity of all the compositions against the bacteria in the form of measuring the inhibition zone created by each nanocomposite in mm. obviously, HAP of low or almost no antibacterial effect, while Li_2O shows the activity of 8.3 ± 0.5 mm against *E. coli* and 8.8 ± 0.6 mm against *S. aureus*. However, adding HAP to Li_2O shows a remarkable enhancement in the antimicrobial activity of 9.6 ± 0.8 mm toward *E. coli* and 9.3 ± 0.9 mm toward *S. aureus*. Further, the antimicrobial activity of HAP/GO is relatively higher than HAP/Li_2O which is 11.3 ± 1 mm and 10.8 ± 1.1 mm, as given in Table 4. The highest antibacterial activity in the assessment is obtained by HAP/Li_2O/GO nanocomposite of 13.4 ± 1.2 mm and 12.3 ± 1.3 mm. Lieb explained the antibacterial activity of Li. This study illustrated the mechanism of antimicrobial activity of Li which is exerted via interfering with microbial replication. A. Mazinani et al. studied the antibacterial effect of GO [82]. They explained that GO exhibited antibacterial activity via the formation of reactive oxygen species. These studies proved the synergistic antibacterial effect of HAP/Li_2O/GO nanocomposite appeared herein our study.

Microhardness study

The resistance of materials toward the indentation refers to their surface hardness. Thus, the topographical changes might play a significant role of the composition's hardness. As obvious in Fig. 11, the value of hardness increased from 2.6 ± 0.1 GPa to 2.8 ± 0.1 and 3.1 ± 0.2 for pure HAP, HAP/GO and HAP/Li_2O/GO, respectively. The improvement of microhardness with the addition of GO is assigned to

Figure 10 Antibacterial activity of HAP, Li_2O, HAP/Li_2O, HAP/GO and HAP/Li_2O/GO: **a** *E. coli*, **b** *S. aureus*, **c** histogram of the obtained numerical results.

Table 4 Different samples based on HAP, TeO_2 and GO and their effect on *E. coli* and *S. aereus*

Composition	*E. coli* (mm)	*S. aureus* (mm)	References
Amoxicillin/CHAP	–	38	[83]
Gentamicin/CHAP	–	28	[83]
Vancomycin/HAP	–	15	[83]
Tobramycin/CHAP	–	27	[83]
Chitosan/PVA/HAP/gold (Au)	13	14	[24]
Chitosan/PVA/HAP/GO/gold (Au)	17	18	[24]
Silver (Ag)/HAP	–	15	[84]
Ag/GO/HAP	–	25	[84]
HAP/GO/CuO	18	15	[85]
HAP/CuO	14	11	[85]
$HAP/Li_2O/GO$	13.4 ± 1.2	12.3 ± 1.3	The current work
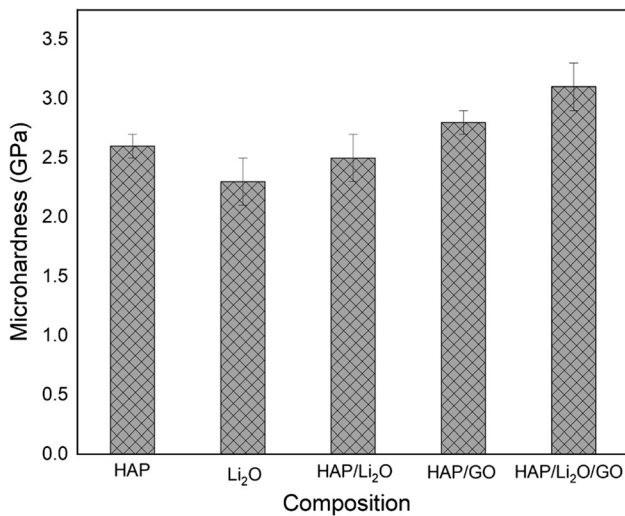
Figure 11 Variation of microhardness of nanocomposites: HAP, Li_2O, HAP/Li_2O, HAP/GO and $HAP/Li_2O/GO$.
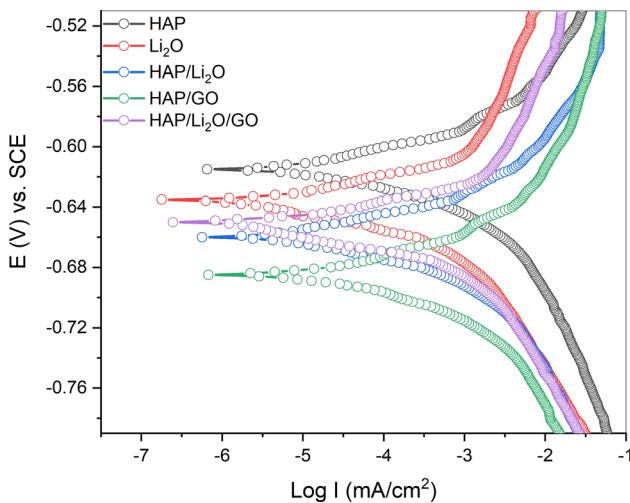
Figure 12 Tafel plot of HAP, Li_2O, HAP/Li_2O, HAP/GO and $HAP/Li_2O/GO$.

GO to combine the HAP's grains together, which might facilitate the dissipation of applied stresses [8, 86]. On the other hand, the difference in particle shape between HAP and Li2O also could promote their dispersibility through the solid solution to inhibit the growth of slipping of dislocations. Further, the mechanical properties could be tailored via compositional variations.

Corrosion study

The Tafel plot of the different nanocomposites is illustrated in Fig. 12. Table 5 represents the different corrosion parameters of the compositions. The corrosion potential (Ec) values were changed from − 0.61 V to − 0.74 V for HAP and $HAP/Li_2O/GO$. The corrosion current (Ic) density varies for each nanocomposite and reaches the lowest value of 0.02 µA for $HAP/Li_2O/GO$. The low Ic value indicates the improvement in corrosion stability of the nanocomposite $HAP/Li_2O/GO$ [47]. Moreover, polarization resistance (Rp) shows a remarkable increase of 385.3 Ohm.cm² for $HAP/Li_2O/GO$. Corrosion resistance plays an important role in the enhancement of the biocompatible ability of the composition, in which the lower corrosion stability shows poor biocompatibility [48]. Besides, the modulation of surface roughness and morphology of $HAP/Li_2O/GO$ is illustrated in the better porous structure and particle size reduction explained in SEM micrographs, significantly improving its corrosion resistance. Therefore, the better corrosion ability of $HAP/Li_2O/GO$ results in improving its biocompatibility so that can be utilized as an implanted biomaterial.

Table 5 Corrosion parameters for HAP, Li$_2$O, HAP/Li$_2$O, HAP/GO and HAP/Li$_2$O/GO obtained from Tafel plot

Compositions	Ec (V)	Ic (mA)	Ba (V)	Bc (V)	Rp (Ohm. cm^2)
HAP	− 0.61	0.05	0.03	0.43	234.24
Li$_2$O	− 0.63	0.12	0.02	0.21	68.56
HAP/Li$_2$O	− 0.65	0.09	0.02	0.16	87.51
HAP/GO	− 0.68	0.07	0.02	0.11	121.24
HAP/Li$_2$O/GO	− 0.64	0.02	0.04	0.06	385.30

Conclusion

Five different nanocomposites are fabricated HAP, Li$_2$O, HAP/Li$_2$O, HAP/GO and HAP/Li$_2$O/GO and examined to be utilized in bone replacement applications. TEM shows the reduction in size and length of nanoparticles after addition to each other with an average 6 nm diameter and 20 nm length for HAP and 6 nm size of Li$_2$O particle. SEM graphs explained the improvement of porous structure and structural alteration of all nanocomposites showing a particle size of 0.3–0.4 μm for HAP/Li$_2$O/GO and a length of 0.8 μm. Besides, HAP/Li$_2$O/GO nanocomposite roughness parameters are noticeably enhanced, showing a roughness average value of 57.80 nm and root mean square roughness, of 75.85 nm. The cell viability of HAP/Li$_2$O/GO was assessed using a human osteoblast cell line to reveal the improvement in biocompatibility and bioactivity, showing a maximum value of 97.4 ± 1.2%. In addition to, the antibacterial evaluation of HAP/Li$_2$O/GO results in high inhibition zone values of 13.4 ± 1.2 mm against *E. coli* and 12.3 ± 1.3 mm against *S. aureus*. Further, the corrosion parameters for the triple composition are enhanced showing a corrosion potential value of − 0.64 V and the corrosion current density value of 0.02 μA. Adding HAP and Li$_2$O to GO sheets results in an improvement in roughness as well as the cell viability, antibacterial activity and corrosion parameters which are explained by different assessments and scans. Hence, HAP/Li$_2$O/GO nanocomposite has better biocompatible and bioactive properties and can be utilized in different bone engineering applications.

Acknowelgement

Funding

Supplementary Information: The online version contains supplementary material available at http s://doi.org/10.1007/s10853-022-07342-1.

References

[1] Wang Y, Zhang W, Yao Q (2021) Copper-based biomaterials for bone and cartilage tissue engineering. J Orthop Translat 29:60–71

[2] Afifi M et al (2022) Improvement of physicochemical properties of ternary nanocomposites based on

hydroxyapatite/CuO/graphene oxide for biomedical usages. Ceram Int 48(3):3993–4004

[3] Jahdaly BAA et al (2021) Tuning the compositional configuration of hydroxyapatite modified with vanadium ions including thermal stability and antibacterial properties. J Mol Struct 1242:130713–130725

[4] Chen S et al (2018) Tuning surface properties of bone biomaterials to manipulate osteoblastic cell adhesion and the signaling pathways for the enhancement of early osseointegration. Colloids Surf B Biointerfaces 164:58–69

[5] Lascano S et al (2020) Graphene-coated Ti-Nb-Ta-Mn foams: A promising approach towards a suitable biomaterial for bone replacement. Surf Coat Technol 401:126250

[6] Fathi AM et al (2021) Taking hydroxyapatite-coated titanium implants two steps forward: surface modification using graphene mesolayers and a hydroxyapatite-reinforced polymeric scaffold. ACS Biomater Sci Eng 7(1):360–372

[7] Jin S et al (2021) Recent advances in PLGA-based biomaterials for bone tissue regeneration. Acta Biomater 127:56–79

[8] El-Naggar ME et al (2021) Microstructure, morphology and physicochemical properties of nanocomposites containing hydroxyapatite/vivianite/graphene oxide for biomedical applications. Luminescence 37:290–301

[9] Khan MUA et al (2021) Development of biopolymeric hybrid scaffold-based on AAc/GO/nHAp/TiO2 nanocomposite for bone tissue engineering: in-vitro analysis. Nanomaterials 11(5):1319–1337

[10] Hartatiek JU et al (2021) Physical and mechanical properties of hydroxyapatite/polyethylene glycol nanocomposites. Mater Today Proc 44:3263–3267

[11] El-Naggar ME, et al (2021) Nanoarchitectonics of Hydroxyapatite/Molybdenum Trioxide/Graphene Oxide Composite for Efficient Antibacterial Activity. J Inorg Organomet Polym Mater

[12] El-Naggar ME et al (2021) Thallium/vanadate co-substitutions through hydroxyapatite/polycaprolactone nanofibrous scaffolds for biomedical domains. Mater Chem Phys 271:124879–124893

[13] Madhavasarma P et al (2020) Studies on physiochemical modifications on biologically important hydroxyapatite materials and their characterization for medical applications. Biophys Chem 267:106474–106485

[14] Ahmed MK et al (2021) Electrospun membranes of cellulose acetate/polyvinylidene difluoride containing Au/Se nanoparticles via laser ablation technique for methylene blue degradation. J Polym Res 28(8):324–333

[15] Ahmed MK et al (2021) Crystal structure optimization, ultrasonic properties and morphology of Mg/Se co-dopant into annealed hydroxyapatite for biomedical applications. J Mater Res 36:1424–1436

[16] Hartatiek et al (2021) Nanostructure, porosity and tensile strength of PVA/Hydroxyapatite composite nanofiber for bone tissue engineering. Mater Today Proc. 44:3203–3206

[17] El-Naggar ME et al (2021) Facile modification of polycaprolactone nanofibers with hydroxyapatite doped with thallium ions for wound and mucosal healing applications. J Market Res 15:2909–2917

[18] Nie W et al (2017) Three-dimensional porous scaffold by self-assembly of reduced graphene oxide and nano-hydroxyapatite composites for bone tissue engineering. Carbon 116:325–337

[19] Nosrati H et al (2019) In situ synthesis of three dimensional graphene-hydroxyapatite nano powders via hydrothermal process. Mater Chem Phys 222:251–255

[20] Khan MUA et al (2021) Development of Biodegradable Bio-Based Composite for Bone Tissue Engineering: Synthesis, Characterization and In Vitro Biocompatible Evaluation. Polym (Basel), **13**(21)

[21] Khan MUA et al (2021) Synthesis and characterization of silver-coated polymeric scaffolds for bone tissue engineering: antibacterial and in vitro evaluation of cytotoxicity and biocompatibility. ACS Omega 6(6):4335–4346

[22] Núñez JD et al (2014) Integration and bioactivity of hydroxyapatite grown on carbon nanotubes and graphene oxide. Carbon 79:590–604

[23] Yu W et al (2016) Design of a novel wound dressing consisting of alginate hydrogel and simvastatin-incorporated mesoporous hydroxyapatite microspheres for cutaneous wound healing. RSC Adv 6(106):104375–104387

[24] Prakash J et al (2020) Nanocomposite chitosan film containing graphene oxide/hydroxyapatite/gold for bone tissue engineering. Int J Biol Macromol 154:62–71

[25] Prongmanee W, Alam I, Asanithi P (2019) Hydroxyapatite/Graphene oxide composite for electrochemical detection of L-Tryptophan. J Taiwan Inst Chem Eng 102:415–423

[26] Santos C et al (2015) Parallel nano-assembling of a multifunctional GO/HapNP coating on ultrahigh-purity magnesium for biodegradable implants. Appl Surf Sci 345:387–393

[27] Rajesh A et al (2019) Probing host-guest interactions in hydroxyapatite intercalated graphene oxide nanocomposite: NMR and scanning probe microscopy studies. Chem Phys Lett 732:136636

[28] Shin YC et al (2015) Synergistic effects of reduced graphene oxide and hydroxyapatite on osteogenic differentiation of MC3T3-E1 preosteoblasts. Carbon 95:1051–1060

[29] Shuai C et al, (2021) *In situ synthesis of hydroxyapatite nanorods on graphene oxide nanosheets and their reinforcement in biopolymer scaffold.* J Adv Res

[30] Moghanian A et al (2018) A comparative study on the in vitro formation of hydroxyapatite, cytotoxicity and antibacterial activity of 58S bioactive glass substituted by Li and Sr. Mater Sci Eng C Mater Biol Appl 91:349–360

[31] Liu L et al (2019) Lithium-containing biomaterials stimulate bone marrow stromal cell-derived exosomal miR-130a secretion to promote angiogenesis. Biomaterials 192:523–536

[32] Hurle K et al, (2021) Osteogenic lithium-doped brushite cements for bone regeneration. Bio Mater

[33] Huang L et al (2021) Lithium chloride promotes osteogenesis and suppresses apoptosis during orthodontic tooth movement in osteoporotic model via regulating autophagy. Bioact Mater 6(10):3074–3084

[34] Wang Y et al (2016) In vitro study on the degradation of lithium-doped hydroxyapatite for bone tissue engineering scaffold. Mater Sci Eng C Mater Biol Appl 66:185–192

[35] Popescu AC et al (2018) Physical-chemical characterization and biological assessment of simple and lithium-doped biological-derived hydroxyapatite thin films for a new generation of metallic implants. Appl Surf Sci 439:724–735

[36] Keikhosravani P et al (2021) Bioactivity and Antibacterial Behaviors of Nanostructured Lithium-Doped Hydroxyapatite for Bone Scaffold Application. Int J Mol Sci 22(17):9214

[37] El-Kader, MFHA et al. (2021) Graphene oxide fillers through polymeric blends of PVC/PVDF using laser ablation technique: electrical, antibacterial, and thermal stability. J Mater Res Technol

[38] Abdel-Wahed MH et al (2020) Structural, optical properties and γ - ray shielding parameters of PbO embedded Li2O borophosphate glass systems. J Non-Cryst Solids 543:120135

[39] Aminitabar M, Amirhosseinian M, Elsa M (2019) Synthesis and in vitro characterization of a gel-derived SiO2-CaO-P2O5-SrO-Li2O bioactive glass. Int J Chem Mol Eng 13(6):296–307

[40] Mansour SF et al (2018) Structure and cell viability of Pd substituted hydroxyapatite nano particles. Biomed Phys Eng Express 4(4):045008–045019

[41] Abdelbar MF et al (2018) Halogen bond triggered aggregation induced emission in an iodinated cyanine dye for ultra sensitive detection of Ag nanoparticles in tap water and agricultural wastewater. RSC Adv 8(43):24617–24626

[42] Zakria MA et al (2020) Ultra-thin silver nanoparticles film prepared via pulsed laser deposition: synthesis, characterization, and its catalytic activity on reduction of 4-nitrophenol. Surfaces and Interfaces 19:100438

[43] Kadu K et al (2019) Role of surface charges on interaction of rod-shaped magnetic hydroxyapatite nanoparticles with protein. Colloids Surf B Biointerfaces 177:362–369

[44] Agalya P et al (2021) Surfactant-assisted microwave synthesis of luminescent/magnetic bifunctional hydroxyapatite nanorods for dual-model imaging. Optik 225:165564–165570

[45] Wadekar PH et al (2020) A novel chemical reduction/co-precipitation method to prepare sulfur functionalized reduced graphene oxide for lithium-sulfur batteries. Electrochim Acta 344:136147–136157

[46] Trivedi MK et al (2015) Physical, atomic and thermal properties of biofield treated lithium powder. J Adv Chem Eng

[47] Chen Q et al (2017) Influence of surface coating on structure and properties of metallic lithium anode for rechargeable Li-O 2 battery. Boletín de la Sociedad Española de Cerámica y Vidrio 56(2):64–72

[48] Anusha T et al (2021) Synthesis and characterization of novel lanthanum nanoparticles-graphene quantum dots coupled with zeolitic imidazolate framework and its electrochemical sensing application towards vitamin D3 deficiency. Colloids Surf A 611:125854–125869

[49] Yang Z et al (2021) Investigation on physicochemical properties of graphene oxide/nano-hydroxyapatite composites and its biomedical applications. J Aust Ceram Soc 57(2):625–633

[50] Zhong J et al (2020) Surface substitution of polyanion to improve structure stability and electrochemical properties of lithium-rich layered cathode oxides. Appl Surf Sci 512:145741–145750

[51] Ding Z et al (2020) Insights into structural characteristics and the mechanism of silicate-based calcium phosphates with phosphoric acid modulation. Ceram Int 46(3):3456–3463

[52] Ucar S et al (2017) Transformation of brushite to hydroxyapatite and effects of alginate additives. J Cryst Growth 468:774–780

[53] Li N-B et al (2016) Rapid deposition of spherical apatite on alkali–heat treated titanium in modified simulated body fluid at high temperature. Surf Coat Technol 301:121–125

[54] Sun Y-H et al (2021) Influence of the Sn(Fe)–C bonds content in SnFe2O4@reduced graphene oxide composites on the electrochemical behavior of lithium-ion batteries. J Alloy Compd 854:157297–157310

[55] Badran H et al (2017) Lithium-doped hydroxyapatite nanocomposites: Synthesis, characterization, gamma attenuation coefficient and dielectric properties. Radiat Phys Chem 130:85–91

[56] Meng W-J et al (2021) Defect-repaired reduced graphene oxide caging silicon nanoparticles for lithium-ion anodes with enhanced reversible capacity and cyclic performance. Electrochim Acta 382:138271–138281

[57] Lala S et al (2014) Biocompatible nanocrystalline natural bonelike carbonated hydroxyapatite synthesized by mechanical alloying in a record minimum time. Mater Sci Eng, C 42:647–656

[58] Tsou HK et al (2012) Improved osteoblast compatibility of medical-grade polyetheretherketone using arc ionplated rutile/anatase titanium dioxide films for spinal implants. J Biomed Mater Res, Part A 100(10):2787–2792

[59] Zhang J et al (2019) The graphene/lanthanum oxide nanocomposites as electrode materials of supercapacitors. J Power Sources 419:99–105

[60] Tsai C-H et al (2019) Synthesis of reduced graphene oxide/macrocyclic ytterbium complex nanocomposites and their application in the counter electrodes of dye-sensitized solar cells. Org Electron 64:166–175

[61] Minale M et al (2021) Hydrous manganese dioxide modified poly(sodium acrylate) hydrogel composite as a novel adsorbent for enhanced removal of tetracycline and lead from water. Chemosphere 272:129902–129914

[62] Zhao WK et al (2021) Removal of formaldehyde by tribo-electric charges enhanced MnO -PI at room temperature. Appl Surf Sci 541:148430–148442

[63] Basfer NM, Mansour SF, Ahmed MK (2021) Physico-chemical properties of hydroxyapatite modified with vanadium ions for degradation of methylene blue. J Mol Struct 1240:130562–130572

[64] Xu X et al (2018) Tunable assembly of porous three-dimensional graphene oxide-corn zein composites with strong mechanical properties for adsorption of rare earth elements. J Taiwan Inst Chem Eng 85:106–114

[65] Vasilescu C et al (2015) Long-term corrosion resistance of new Ti–Ta–Zr alloy in simulated physiological fluids by electrochemical and surface analysis methods. Corros Sci 93:310–323

[66] Tonks JP et al (2017) Corrosion studies of LiH thin films. J Nucl Mater 484:228–235

[67] Shalan AE et al (2021) Electrospun nanofibrous membranes of cellulose acetate containing hydroxyapatite co-doped with Ag/Fe: morphological features, antibacterial activity and degradation of methylene blue in aqueous solution. New J Chem 45(20):9212–9220

[68] Ramadan R, Ahmed MK, Uskoković V (2021) Magnetic, microstructural and photoactivated antibacterial features of nanostructured Co–Zn ferrites of different chemical and phase compositions. J Alloy Compd 856:157013–157028

[69] Abdel-Hakim A et al (2021) Acoustic, ultrasonic, mechanical properties and biodegradability of sawdust/ recycled expanded polystyrene eco-friendly composites. Polym Testing 99:107215–107224

[70] Ahmed MK et al, (2020) Pb(II) and Cd(II) removal, mechanical and morphological features of nanofibrous membranes of cellulose acetate containing fillers of hydroxyapatite, graphene oxide, and magnetite. Applied Physics A. **126**(10)

[71] Menazea AA, Ahmed MK (2020) Wound healing activity of Chitosan/Polyvinyl Alcohol embedded by gold nanoparticles prepared by nanosecond laser ablation. J Mol Struct 1217:128401–128410

[72] Menazea AA, Ahmed MK (2020) Nanosecond laser ablation assisted the enhancement of antibacterial activity of copper oxide nano particles embedded though polyethylene oxide/ Polyvinyl pyrrolidone blend matrix. Radiat Phys Chem 174:108911

[73] Menazea AA, Ahmed MK (2020) Silver and copper oxide nanoparticles-decorated graphene oxide via pulsed laser ablation technique: Preparation, characterization, and photoactivated antibacterial activity. Nano-Structures & Nano-Objects 22:100464

[74] Donya H, Darwesh R, Ahmed MK (2021) Morphological features and mechanical properties of nanofibers scaffolds of polylactic acid modified with hydroxyapatite/CdSe for wound healing applications. Int J Biol Macromol 186:897–908

[75] Müller B (2010) Tailoring biocompatibility: BENEFITTING patients. Mater today 13:58–60

[76] Zayed MA et al (2020) Morphological and magnetic features of Ru(III) doped magnetite ultrafine nanoparticles. Mater Res Express 7(12):125002

[77] Wu VM et al (2020) Empirical and theoretical insights into the structural effects of selenite doping in hydroxyapatite and the ensuing inhibition of osteoclasts. Mater Sci Eng C Mater Biol Appl 117:111257–111277

[78] Ahmed MK et al (2021) Morphological behaviors of brushite/vivianite nanocomposites and their potency for Se(IV) and Cd(II) removal from aqueous solutions. Mater Chem Phys 259:124057

[79] Kyrkjebø S et al (2021) Graphene and graphene oxide on Ir(111) are transparent to wetting but not to icing. Carbon 174:396–403

[80] Adhikari J et al (2021) Development of hydroxyapatite reinforced alginate–chitosan based printable biomaterial-ink. Nano-Struct Nano-Objects 25:100630

[81] Arioka M et al (2014) Acceleration of bone regeneration by local application of lithium: Wnt signal-mediated

osteoblastogenesis and Wnt signal-independent suppression of osteoclastogenesis. Biochem Pharmacol 90(4):397–405

[82] Mazinani A et al (2021) Graphene oxide (GO) decorated on multi-structured porous titania fabricated by plasma electrolytic oxidation (PEO) for enhanced antibacterial performance. Mater Des 200:109443

[83] Stigter M et al (2004) Incorporation of different antibiotics into carbonated hydroxyapatite coatings on titanium implants, release and antibiotic efficacy. J Control Release 99(1):127–137

[84] Yahia IS, Shkir M, Keshk SMAS (2020) Physicochemical properties of a nanocomposite (graphene oxide-hydroxyapatite-cellulose) immobilized by Ag nanoparticles for biomedical applications. Results Phys 16:102990

[85] Afifi M et al (2021) Improvement of physicochemical properties of ternary nanocomposites based on hydroxyapatite/CuO/graphene oxide for biomedical usages. Ceram Int 48:3993–4004

[86] El-Naggar ME et al (2021) Tailoring combinations of hydroxyapatite/cadmium selenite/graphene oxide based on their structure, morphology, and antibacterial activity. J Inorg Organomet Polym Mater 32:311–325